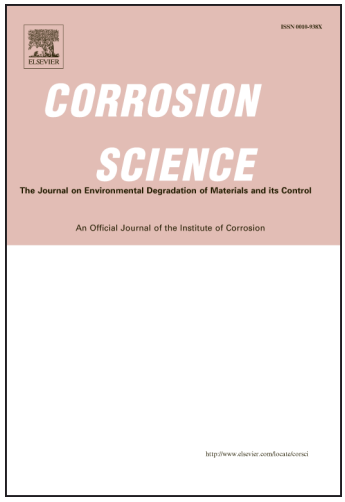

Establishing a Correlation between Interfacial Microstructures and Corrosion Initiation Sites in Al/Cu Joints by SEM-EDS and AFM-SKPFM

M. Sarvghad-Moghaddam, R. Parvizi, A. Davoodi, M. Haddad-Sabzevar, A. Imani

PII: S0010-938X(13)00469-1
DOI: http://dx.doi.org/10.1016/j.corsci.2013.10.039
Reference: CS 5586

To appear in: *Corrosion Science*

Received Date: 28 May 2013
Accepted Date: 31 October 2013

Please cite this article as: M. Sarvghad-Moghaddam, R. Parvizi, A. Davoodi, M. Haddad-Sabzevar, A. Imani, Establishing a Correlation between Interfacial Microstructures and Corrosion Initiation Sites in Al/Cu Joints by SEM-EDS and AFM-SKPFM, *Corrosion Science* (2013), doi: http://dx.doi.org/10.1016/j.corsci.2013.10.039

Establishing a Correlation between Interfacial Microstructures and Corrosion Initiation Sites in Al/Cu Joints by SEM-EDS and AFM-SKPFM

M. Sarvghad-Moghaddam[1], R. Parvizi[1,2*], A. Davoodi[3], M. Haddad-Sabzevar[1], A. Imani[3]

[1]*Metallurgical and Materials Engineering Department, Ferdowsi University of Mashhad, Mashhad 91775-1111, Iran.*

[2*]*School of Engineering, Faculty of Science and Technology, Deakin University, Victoria 3220, Australia.*

[3]*Materials Engineering Department, Hakim Sabzevari University, Sabzevar 391, Iran.*

Abstract

A lap joint of AA3003 and pure copper was produced by friction stir welding and the induced interfaces were investigated. Interfacial regions were characterized by SEM-EDS, AFM, SKPFM, OM and Vickers micro-hardness. Multimodal Gaussian distribution (for characterization of surface potential patterns) showed the formation of multiple compounds. A quantitative correlation between microstructure constituents and Volta potential distribution was recognized and confirmed by corrosion attacked sites observations. It was observed that the Al-rich regions proximate the dispersed Cu particles and Cu-Al intermetallics were most susceptible to corrosion attack initiation due to a galvanic driving force between these surface constituents.

* Corresponding author, Tel/Fax: +61352272167, Email(s): parvizi.reza@gmail.com, rparvizi@deakin.edu.au

Keywords: A. Intermetallics; B. AFM; B. SEM; C. Interfaces; C. Pitting corrosion; C. Welding.

1. Introduction

Aluminum/copper bimetals are usually considered of high interest to electrical, aerospace, shipbuilding, and other industrial applications [1-2]. As the fusion welding of this dissimilar couple is difficult due to the formation of brittle intermetallic compounds (IMCs), friction stir welding (FSW) is considered to be an alternate process [3-11]. An investigation by Elrefaey et al. [12] on FS welded Al/Cu lap joints of AA1100-H24 to copper with a double-shoulder design showed different zones in the weld including stirred zone (SZ) and heat affected zone (HAZ); without any thermo-mechanically affected zone (TMAZ). Another study by Saeid et al. [8], demonstrated the formation of HAZ and TMAZ affected by the formation of IMCs and micro-cracks as a result of heat-input at various welding speeds. Similar studies revealed different IMCs of CuAl, $CuAl_2$, $CuAl_4$, and Cu_9Al_4 with a brittle nature close to the Al/Cu interface [6-7, 9, 12-13]. Xue et al. [9] showed that an excellent metallurgical bonding between aluminum and copper at the Al/Cu interface may be achieved because of the formation of a continuous and uniform Al–Cu intermetallic layer with a proper thickness of about 1 μm. It is also reported that, severe plastic deformation and thermal exposure facilitate the formation of IMCs [7, 10-11]. A survey by Galvão et al. [10] also represented the formation of mixed regions of aluminum, copper, $CuAl_2$ and Cu_9Al_4 with heterogeneous structures and intermetallic content along the Al/Cu interface. Other studies [14-15] report that, during welding, copper segregates to grain boundaries and causes the $CuAl_2$

IMC to form through the eutectic reaction of: liquid → $CuAl_2$ (or θ phase) + α (Al-rich solid solution). As these Cu-rich IMCs act as micro-cathodes, the surrounding α-phase dendrites become susceptible to corrosion. Transmission electron microscopy (TEM) observation by Feng et al. [16] in a friction stir processed AA2219-T6 alloy attributed the presence of equilibrium θ to the followings:

a) Dwelling at above 480°C leads the semi-coherent θ′ precipitates and plate-shaped coherent θ″ metastable precipitates overage to the equilibrium θ phase.

b) Having heated above the solvus temperature (513°C), the metastable precipitates dissolve into the matrix and reprecipitate as equilibrium θ phase upon slow cooling rate behind the tool.

However, understanding the material affinity to corrosion and characterization of such an interface would be easier by employing multiple complementary techniques. Recently, scanning Kelvin probe force microscopy (SKPFM) is developed for concurrent mapping of topography and Volta potential distribution on metal surfaces in the air [17-25]. It combines the classical Kelvin probe technique with atomic force microscopy (AFM). Recently, this method has been advanced to investigate the corrosion processes under atmospheric weathering conditions on a micro or even nano-scale and has a high resolution of c.a. 1 mV in reading the surface potential [26]. The outlining of the surface Volta potential of a sample is made by employing a two-pass technique; i.e. each line of the image is scanned twice. In the first step of each scan, external voltage is not applied to the tip instead line topography is recorded using the tapping mode technique (that oscillates near the tip resonant frequency of 150-175 kHz by a Piezoelectric tool) and AFM mapping of the topography image from the sample surface. This data is then used during the second pass of scanning where a DC bias

potential and an oscillating AC potential with a frequency equal to the resonant frequency of the cantilever is applied to the tip. The tip is then lifted to a selected distance and a feedback loop that controls the Z Piezo-element is turned off during the second pass. Hence, the mapping of surface potential and topography is done line by line at the same time [17].

To the present, although a number of complementary techniques have been used to describe the microstructural characteristics of FS welded joints [27], there is a paucity of research carried on the nature of the interface and its characteristics in dissimilar joints. Thus, the aim of this research is devoted to combine diverse techniques including scanning electron microscopy-energy dispersive spectroscopy (SEM-EDS), AFM, SKPFM, optical microscopy (OM) and Vickers micro hardness to better characterize the Al/Cu bimetal interface. Particularly, an attempt was performed to quantitatively find out a correlation between the namely mentioned techniques in investigating the interface characteristics of an FS welded Al/Cu joint. Indeed, such information will direct one to a consistent idea of corrosion initiation sites at the induced interfaces.

2. Experimental procedure

2.1. Welding procedure

An FSW adapted milling machine was employed for the welding procedure providing 1100 rpm and 50 mm/min rotation and welding feed (traverse) speeds, respectively. The process was carried out on a lap joint of an 8 mm thick plate of 3003 aluminum alloy on top and a 5 mm thick commercially pure copper at the bottom. The chemical composition of the aluminum plate was (in wt%): 1.292% Mn, 0.652% Fe, 0.157% Si,

0.124% Cu, 0.038% Mg, 0.024% Sb, 0.017% Cr, 0.011% Ti, 0.011% Zn, 0.005% Sn and Al as balance. The copper plate also consisted of (in wt%): 0.053% Al, 0.018% Fe, 0.011% Zn, 0.007% Pb, 0.006% P, 0.005% Sn, 0.003% Mn, 0.003% Mg, 0.002% Si, and Cu as balance. Both plates were cut into 20 cm × 20 cm pieces and subjected to FSW using H13 hot work double-shoulder steel tool as introduced by Brooker et al. [7]. The tool was designed to be located at the interface between the two pieces being welded. The welding tool itself consisted of a lower 10 mm diameter and an upper 40 mm diameter concave shoulders with coaxial circular treads (scrolled-like configuration) and a primary lower tapered, parallel- treaded pin of 3 mm length beneath a secondary conic pin of 8 mm length with parallel treads (Fig. 1a). In this figure, a real optical image of the weld cross section is attached to the schematic illustration for better clarification. In the current study, the words “pin” and “shoulder” refer to the primary lower pin and the lower shoulder, respectively. Not having provided a pre-drilling start hole, the pin end initially penetrated through the top aluminum plate, and extended up to 3 mm into the bottom copper plate, whilst the tilting angle was set to 1.5°. Due to high thermal conductivity of copper, the work piece was preheated up to 200 °C prior to welding. To obtain an entirely welded interface (in order to completely surf the welding area and form a fully welded Al/Cu interface), the weld was implemented by performing a multi-pass technique with an offset distance of 8 mm between parallel weld passes that caused a 2 mm overlap between adjacent weld lines (Fig. 1a).

2.2. Sample preparation

In order to provide a suitable section for AFM, SKPFM, SEM-EDS, OM and micro hardness studies, a cutoff cross-section from the weld was selected, degreased by

acetone, mechanically wet polished down to 0.05 μm alumina slurry, washed with ethanol and finally dried by hot air blow. Fig. 1b reveals an SEM illustration of the three different regions investigated in this study. The P1 region corresponds to the region around the pin while the S1 region refers to the area beneath the shoulder. The P2 region, adjacent to P1, also depicts the area around the pin on which some complementary analyses were performed. Note that all the mentioned experiments have been performed on just one mirror-like surface.

2.3. Macro and microstructural investigation

Macro and microstructural changes from copper to the aluminum matrix (at both the as-polished and etched conditions) were examined using a digital camera and SEM (model: LEO 1450 VP, resolution: 2.5 nm, Max voltage: 35 kV) equipped with secondary electron (SE) and EDS analysis system (resolution: 133 eV). EDS line-scans in the P1 and S1 regions were performed to study the chemical composition transition from Cu to Al matrixes. In all backscattered SEM images, light and dark phases are related to copper and aluminum containing components, respectively. The gray colored components are those intermediate compositions consisting of both Cu and Al elements (together with other accompanying minor alloying elements).

2.4. Topography and Volta potential analysis

Topography and Volta potential images were taken using a commercial Solver Next AFM instrument (from the NT-MDT Co.) from the mirror-like polished surface. All mappings were performed in the air at room temperature with relative humidity between 20 and 30 percent [18]. The AFM tip was a pyramid single crystal silicon, n-type with

antimony doped and coated by conductive PtIr (25 nm) and Cr adhesive layer (2.5 nm). For Volta potential mapping, the lift scan height was about 30-50 nm (depending on the surface roughness), where the effects of dipole charges close to the surface were believed to be minor. Topography and Volta potentials were scanned with a pixel resolution of 256 × 256 and a scan frequency rate of 0.5 Hz. The luminosity of different zones in topographic images shown in this investigation corresponds to the different heights of features on the sample surface. Shiny zones are higher than dark ones on the topographic maps. In a comparable way, the brightness on Volta potential images was cooperated with different Volta potentials of the features shown on the Volta potential map. Bright areas have higher Volta potentials than dark areas. One important aspect related to the working principle of the SKPFM is that it is possible to measure Volta potential differences for any individual scanning of the sample surface. This issue is particularly important for Volta potential data interpretation [17, 28]. Therefore, the sample Volta potentials that were always measured concerning the surrounding matrix and the relative values could only be used as comparison on an individual sample surface.

To interpret the Volta potential values analytically, histogram plots of SKPFM images were extracted and the multimodal Gaussian distribution of corresponding spectrums acquired. Equation 1 shows a single Gaussian (normal) distribution function:

$$y = \frac{1}{\sigma\sqrt{\pi/2}} \exp\left[-\frac{2(x-\mu)^2}{\sigma^2}\right] \qquad (1)$$

where, y represents the counts number, σ is the standard deviation, x refers to the Volta potential value and μ is the mean value parameter. In order to estimate the number of multimodal distribution peaks (the number of events probability), the first derivatives of

the histograms and their inflection points are calculated. All SKPFM data were presented as real measured instead of inverting images [28].

2.5. Corrosion investigation

To study the corrosion attack morphology or preferentially attacked sites, the same polished sample was immersed in a 1 M HCl solution for 30 seconds. During this period, the sample surface was continuously checked (for three times) by using an optical microscope. The best exposure time to reveal the initially attacked sites was chosen to be 30 seconds. After each extraction, the sample was washed with ethanol, cleaned for 5 minutes in an ultrasonic cleaner and subsequently dried by hot air blow. Afterwards, OM and SEM were utilized to scrutinize the corrosion attack sites.

Vickers micro hardness test was done (as the last experimental procedure on the sample surface) using a Buehler micro hardness machine (load= 50 gr, dwell time= 10 s, center-to-center spacing= 50 and 200 µm) on the cross-section of the joint perpendicular to the welding direction. Two linear hardness profiles were probed along the P1 and S1 regions.

3. Results and discussion

3.1. Hardness

Fig. 2 demonstrates the Vickers micro hardness profile along straight lines in the P1 and S1 regions. The hardness values measured in P1 (around the pin), show that while the hardness of Cu remains nearly constant by a 50 µm distance from the interface (about 89 HV), a sudden rise occurs at the interface (about 201 HV). Similar to another

experiment, no significant HAZ could be observed in this region due to the high heat sink rate of the copper matrix as a consequence of its high thermal conductivity [7]. On the other hand, in the Al side, a gradual diminution in hardness occurs by furthering from the interface, which reaches c.a. 47 HV in more distant areas. Concerning the melting temperature of Al (660.3 °C), its thermal conductivity (237 $W.m^{-1}.K^{-1}$), the induced plastic deformation and dynamic recovery the alloy shows a lower hardness value in comparison with the adjacent copper alloy in P1. In addition, it should be mentioned that the absence of HAZ in this Al-rich region could also be due to the high rates of plastic deformation and material turbulence. In this case, a similar TEM observation by Sato et al. [29] indicated that the reduction in hardness values could be attributed to the transition of dislocation cell structure to a sub-grain structure with relatively low dislocation density as a result of dynamic recovery in this region during the FSW process.

For the S1 region, a different behavior is evident. Hardness values show a dramatic surge at the Al/Cu interface (c.a. 353 HV), while a slight increase can be seen by furthering from Al/Cu interface (about 100 μm) into both matrixes (c.a. 137 HV on both sides). By advancing from the interface to the Cu matrix, a hardness value of about 87 HV is acquired. On the Al side, a similar behavior is detectable and a hardness value of about 110 HV is achieved for the last measured point. As can be seen, the overall hardness in the P1 region is lower than that of the S1 at both the interface and the Al side. The two maxima, 353 and 201 HV are observed exactly at the interface. It is also interesting to note that the zone with a high hardness value does not extend more than 100 μm. These results confirm the fact that, although the transition region is relatively narrow (c.a. 50 μm - the dashed rectangular area in Fig. 2), FSW has dramatically

altered the hardness characteristics of both materials at the interface. At the both S1 and P1 regions, the relatively high hardness values at and near the interfaces are much higher than those of the Al and Cu base matrixes. Therefore, the particles in these areas should be Al-Cu IMCs rather than Cu or Al-rich phases [9]. Moreover, the higher hardness values at the Al side in S1 in comparison with those of the P1 could be attributed to the higher amounts of plastic deformation (between the two shoulders; see Fig. 1a) and the consequent strengthening mechanisms (e.g. grain refinement). In other words, the aluminum in S1 undergoes the concurrent impacts of the both shoulders and that of the upper pin. In such a condition, the tool induces more severe plastic deformation in the S1 region in comparison with the P1 region (that is just influenced by the lower pin and shoulder). It has been reported that the scrolled geometry of shoulder provides greater grain refinement in the S1 region [30-32]. Beygi et al. [33] also stated that the lack of Al traces due to the downward material movement and that the S1 interface experiences a severe plastic deformation with no occurrence of recrystallization, lead to higher hardness values in the S1 region. According to our results, it seems that the tool shoulder has a dominant impact on the interface hardness in the S1 region. The same behavior can be observed between the Cu sides of the two regions, especially at the interfaces.

Correspondingly, these high hardness values at interfaces might be attributed to several factors. These may include the formation of solid solutions and IMCs, grain refinement, reduction in dynamic recovery/recrystallization, the higher densities of defects like dislocations and their roles in work hardening mechanisms (e.g. Orowan strengthening mechanism) [1-2, 9, 16, 29, 33-40]. Comparing this research with the literature, it can be deduced that the slight difference in hardness values of the S1 region in the Cu side

can be attributed to the formation of a narrow HAZ, grain growth or the absence of banded microstructure [33-34]. It should be noted that, as the majority of the generated heat in FSW comes from the tool shoulder (only 14 percent of the heat is created by the tool pin [30]), the formation of a slim HAZ in S1 seems quite possible. SEM-EDS images taken from the mentioned regions confirm the existence of IMCs of Al and Cu at the interfaces; the results will be discussed in the next section.

3.2. SEM-EDS analysis

Fig. 3 illustrates the SEM-BSE images with the inserted line-scan results (in at%) in the P1 and S1 regions. In the P1 region, four distinct constituents are detectable: a Cu-rich matrix, a transition layer at the interfacial region, an Al-rich phase (dark/black in color) surrounded by dispersed IMCs and scattered Cu particles (bright white color) in the Al matrix (Fig. 3a and 3b). Concerning the literature and the current results, the presence of these unaffected Cu particles adjacent to the aluminium matrix (around the pin) indicates that they did not reach the Al/Cu threshold reaction temperature [11, 13, 16]. EDS analysis reveals that these phases are mainly composed of Al, Cu and Zn elements distributed along the interface to the both matrixes. Fig. 3b depicts a high magnification image adjacent to the transition layer in P1. As it can be easily seen, by approaching the copper side at the interface, a Cu-Al-Zn containing transition layer (the light grey layer) appears in different thicknesses (with an average thickness of about 2 μm) all along the interface. The corresponding metallic contents (in at%) of this layer can be found in Table 1 data. Previously, it has been reported that this layer could be constituted of either an Al_4Cu_3Zn (denoted as τ) IMC or an Al-Cu-Zn solid solution [41]. However, considering its homogeneous structure and the variation in its constituent elements, it seems to be a solid solution rather than an IMC. Disappearance of this diffusion layer in

more distant areas can be attributed to the lack of diffusion and the limited solubility of aluminum in copper; this has also been pointed out elsewhere [14, 41-42]. Indeed, this feature can be arisen from variable diffusion conditions at dissimilar areas along the interface. It is believed that this can be attributed to different impacts of the tool pin and shoulder in dispersing the two major sources of induced heat (heat-input), severe plastic deformation and friction, along the induced interfaces [10, 30, 35]. With that in mind, these compositional/morphological variations can bring on a complex corrosion behavior in the welded areas.

To characterize the S1 region, EDS line-scan analysis (in at%) was carried out from the locations marked in Fig. 1b and the outcome is shown in Fig. 3c. Results show the existence of dispersed Al-Cu IMCs in the α eutectic at/around the interface. Moreover, it is obvious that the eutectic area in S1 (with somehow different microstructure; see Fig. 8) is more extended (about four times) in some regions in comparison with the P1 region. In agreement with the literature, this can be accredited to the higher amount of plastic deformation and subsequent generated heat that supports elemental diffusion (migration) through the interface [9-10, 36, 43]. Formerly, Galvão et al. [10] stated that as aluminum is quite softer than copper, there are constrained remnants of Al inside the conical shaped scrape volume under the shoulder (where an Al-rich mixing volume is formed). Moreover, they mentioned that this can be the reason for the presence of large amounts of $CuAl_2$ at the top layer of the interface that consists of an IMC-rich matrix. On the other side, assuming the temperature across the interface to be around 500°C, the Cu to Al and Al to Cu diffusion coefficients (D_{Cu-Al} and D_{Al-Cu}, respectively) are reported to be 4.1×10^{-14} and 2.9×10^{-14} $m^2.s^{-1}$, respectively [42, 44]. Considering these

values and the physical states (e.g. solid or semi-solid) of the Cu and Al elements close to the interface, it can be deduced that the diffusion of Cu atoms into the Al matrix would be much easier than that of the Al atoms into the Cu matrix. Therefore, this may be why the observable eutectic phase would tend to extend in the Al matrix rather than in the Cu one. Interestingly, considerable fluctuations are observed in the line-scan of both Al and Cu elements (particularly for Al) while passing through the eutectic phase. This denotes that there is a noticeable difference in the Al content of eutectic constituent phases. The structural details of this phase in these regions (S1 and P1) are well illustrated in Fig. 8, which will be discussed later.

To investigate the pin rotation/traverse effect on the Al/Cu interface, EDS was conducted on nine points (approximately aligned) in the P2 region (Fig. 4). Table 1 shows the chemical composition (in at%) results of each spectrum. Note that the EDS results may not represent exactly the real composition of the analyzed points, but can be used as acceptable estimation. A comparison between the atomic percentages of Cu, Al and other major elements is illustrated in Fig. 4b bar-chart that reveals the presence of IMCs such as $CuAl_2$ and $Al_6(Mn,Fe)$ in this region. Similar IMCs have been reported to be found in similar works by other researchers [9, 13, 45]. Spectrum 1 shows the composition of the aluminium matrix in the SZ of P2 while spectrum 2 reveals the chemical composition of an unaffected IMC (probably $Al_6(Mn,Fe)$) in the Al matrix; see Table 1. Moreover, a kind of very small IMC (possibly $Al_{15}(Mn,Fe)_3Si_2$ [45]) is detectable outside the two-phase zone. Spectrum 3 demonstrates an Al/Cu IMC in the transition zone maybe of $CuAl_2$ type (also see Table 1 data). Spectrum 4 depicts the composition of the Al-rich eutectic phase containing some amounts of Cu, Fe, Mn and Zn elements. Spectrum 5 represents the composition of the semi-homogeneous gray

eutectic phase with trace amount of Mn element. Relatively coarse IMCs with this composition are clearly observed at this transitional zone. Spectrums 6 to 9 illustrate the composition change of the Cu, Al and Zn elements by furthering from the interface. Regarding the Al-Cu-Zn phase diagram (miscibility gap of Zn in Al [41]) and Zn diffusion coefficients (at 500°C) in Al and Cu matrixes (D_{Zn-Al}= 4.86 × 10^{-14} and D_{Zn-Cu}= 4.0 × 10^{-18} $m^2.s^{-1}$ [41-42, 46]), it is expected that Zn partitioning occurs by approaching the Al/Cu interface from the Al-rich side; see Fig. 4b. On the other side, it is obvious that Al concentration gradually diminishes by approaching the Cu matrix. This finding is completely in agreement with the literature reporting the formation of Cu-Al-Zn solid solution in a Cu matrix [6, 11, 14, 34, 41]. Considering previous works, the presence of various Al-Cu based IMCs like CuAl, $CuAl_2$, Cu_9Al_4, and some other compounds containing various amounts of Al, Cu, Mn, Fe and Zn is possible in this complex area [6, 9-10, 43-44, 47]. However, the exact nature of some constituents is not clearly understood. For instance, in a research it has been suggested that although many small Cu particles are expected to transform to IMCs, limited and very small formed eutectic particles are likely to be dissolved during FSW [14]. However, in this work, some other types of unreacted Cu particles are also observed at various sizes/shapes in the Al-rich SZ adjacent to the tool pin. Because of the multi-pass FSW process, divergent thermal profiles, geometrical parameters of the joint and the long exposure of the work piece to elevated temperature, complex interactions/reactions between Al and Cu elements seems plausible. Therefore, a diverse range of galvanic driving forces between these constituent phases and consequently different local sites prone to

corrosion initiation will be built up. More details in SEM microstructural characterizations are discussed in the next section.

3.3. SKPFM, AFM and localized corrosion attack analysis

Fig. 5 shows SKPFM results captured from the P1 region. A camera view of the whole scan region is shown in Fig. 5h. Imaging was performed by sweeping from the Al side to the interface and then into the Cu texture. AFM results of the S1 and P1 regions (in as polished state) are not shown here since they indicate nearly the same outcome. To cover up the entire area, seven individual scanning steps (50 by 50 micron) were accomplished. Normally, line profile is used to evaluate the Volta potential and topographical variations on surfaces [17-18, 20-23, 26, 28, 48-49]. However, this process does not seem to be suitable for quantitative comparison of different images [50]. In the present work, in order to interpret the results carefully, histogram plots and associated multinomial distribution functions of Volta potential variations are extracted and shown in Fig. 5i. Four parameters are usually considered for quantitative evaluation of the acquired data: The number of multinomial distribution peaks, the corresponding mean value (μ), standard deviation (σ) and half width of the spectrum ($\omega/2$) [50]. The number of multinomial distribution peaks is used to identify the number of event probabilities; in the present research, these peaks represent the number of surface constituents. The difference between the mean values (Volta potential difference) is used to evaluate the galvanic driving force for corrosion initiation while the standard deviation was implemented for homogeneity evaluation of surface constituents. The similar procedure has been complemented elsewhere [17, 23, 45]. The half widths of the spectrums, finally, illustrate the variation of Volta potential value for each individual constituent. Table 2 shows the extracted multimodal Gaussian distribution parameters (σ

and μ) from Volta potential histograms (Figs. 5, 6 and 7). According to the mean values of Volta potential (575 and 35 mV for Al and Cu, respectively) corresponding to the peaks in "a" and "g" curves in Fig. 5i, Al containing phases represent higher real measured Volta potential values. While a normal (Gaussian) distribution Volta potential variation is applicable to the pure Cu side (also a narrow standard deviation as an indication of reasonable surface homogeneity), the presence of IMCs causes a deviation from the single normal distribution on the Al side. This means that the tail on the left side of the Al alloy histogram corresponds to the Volta potential values of IMCs; see Fig. 5i and a. Moreover, Al shows greater standard deviation on Volta potential due to the presence of more surface heterogeneities. The small black spots with lower potentials in this figure are mainly attributed to the alloy inherent IMCs (mainly Al_6(Mn,Fe)). Quite similar results have been observed in previous works for the AA3003 alloy [45, 51].

The histogram corresponding to Fig. 5b indicates a bimodal distribution, demonstrating the presence of two individual constituents. The asymmetric bimodal distribution points to the presence of at least one new component. The left side seems to be related to unreacted Cu particles and the right side can be associated to Al alloy compounds. Note that in this figure, the lately mentioned black spots (in Fig. 5a) are brighter in color due to the presence of more cathodic sites (Cu particles) with much lower absolute Volta potential values. The difference between the two related mean values of Volta potential obtained by bimodal distribution (i.e. 650 mV from pick to pick) can be an indication of a noteworthy driving force for micro-galvanic corrosion that is in agreement with literature [17, 21, 48, 52]. Therefore, it is judged that the micro-galvanic corrosion initiates preferentially from the interface of a region with such potential differences.

This is confirmed by SEM images taken after exposure to 1 M HCl corrosive media, which will be discussed later. Interestingly, the mean value of the right side constituents is even higher than that of the Al alloy itself. At the first glance, it may seem that some new components were formed between Al and Cu matrixes. But, comparing with previous researches, this can be ascribed to the respective measurement of the surface potential by SKPFM in the presence of new surface constituents [17, 20, 48]. Generally, it is notable that elements such as Fe, Mn and Zn are nobler than Al in either their free states (if probable) or in their reacted states; like IMCs [23, 45]. Therefore, it is expected that corrosion preferably initiates from Al-rich/secondary phase interfaces. By gradually moving from the Al matrix to Cu, mean potential values shift toward the Cu component. In Fig. 5c, it is obvious that Cu particles are refined and dispersed because of the severe turbulence around the tool pin. Also, some brownish components are observed in this region that can be related to Cu-Al IMCs (like θ-$CuAl_2$ in the eutectic phase). By advancing from the Al side to the Al/Cu interface, the amount of this phase increases. This is while the amount (or number) of Cu compounds (black spots) decreases contrarily (Fig. 5c, 5d and 5e). Concerning Fig. 5f, five distinct constituents are detected; Cu particles, dark eutectic phase, bright eutectic phase, transition zone and the Cu matrix. The difference between these eutectic phases can be attributed to the partitioning of solute atoms like Zn. In other words, a concurrent depletion/enrichment mechanism occurs at the vicinity of interfacial regions. It can be inferred from other researches that such an inter-diffusion around the pin might be mainly due to the formation of a mechanical mixture at high deformation rates, elevated temperatures and a sufficient time span during FSW [42, 44, 46].

It is also worth to mention that Volta potential distribution in the interfacial region follows a multimodal distribution pattern that may be due to the formation of several constituents. Again, the presence of five components is confirmed since there are multinomial (quinquemodal) distributions in the histogram of Fig. 5f. Their compositions vary from the Al rich compounds from one side to the Cu rich compounds on the other side; details are represented in Fig. 5j. Considering the potential values of these constituents, a complicated corrosion pattern will be introduced after exposure to the aqueous environment. These verdicts are completely consistent with SEM-EDS results in Fig. 4 (with the same interpretation for elemental (e.g. Zn) partitioning).

Fig. 6 shows the sequential Volta potential images starting from the Al matrix to Cu in the S1 region. Fig. 6b shows some Al-rich islands that are surrounded by the eutectic phase. It should be mentioned that the morphology of the eutectic phase in this region is different from the one in P1. This has been attributed to various mechanical and thermal treatment history of this area during the welding process [10, 16, 30, 47]. Here, in Fig. 6e, surface constituents are the same as those found in Fig. 5f. In addition, the same multinomial distribution details are extracted for the Fig. 6c histogram (Fig. 6h). Although similar normal, bimodal and multimodal distributions can be applied to the quantitative analyzing Volta potential values, there is a meaningful difference between Volta potential variations around the pin (Fig. 5) and beneath the shoulder (Fig. 6). The highest Volta potential difference of c.a. 350 mV can be observed in Fig. 6b (200 and 550 mV corresponding to Cu and Al sides, respectively). This is lower than the 700 mV span in Fig. 5b, which means that corrosion is more likely to be initiated from the areas that are affected by the tool pin. Moreover, while the Volta potential mean values of the Cu surface on the both pin and shoulder regions (Figs. 5i and 6g) are almost similar (c.a.

35 mV), the real measured mean Volta potential values on the Al side are different in P1 and S1 regions. Thus, it can be concluded that the galvanic driving force for corrosion origination is highest in the P1 region. Compared to the previous results, the reason can be attributed to the higher thermal gradient, more material flow, plastic deformation and enhanced depletion/enrichment mechanism beneath the shoulder in contrast with the area around the pin. Therefore, the eutectic phase is expected to be more extended in the S1 region in comparison with the P1 and P2 regions (Figs. 3 and 4). It should be mentioned that the micro-galvanic corrosion may also occur locally at regions revealing the highest Volta potential values (Fig. 6b), i.e. the area beneath the shoulder. Comparing the Figs. 5 and 6, a dendritically grown microstructure is detectable (entertainingly revealed by scanning the surface Volta potential) beneath the shoulder. In agreement with other works, no significant dendritic growth could be observed around the pin region because of crumbling during the tool pin movement [6, 36]. A direct evidence for this dendritic-like and refined structure is shown in OM and SEM images of Figs. 7 and 8. Furthermore, it is obvious that in both regions, the major interfacial constituents are Cu-Al compounds and the mean values of Volta potential are closer to those of the Cu side; see Figs. 5e, 5f, 6d, 6e and their corresponding histograms.

Fig. 7 displays OM, SEM, AFM and SKPFM (together with a line-scan and a multinomial distribution histogram) images of the P2 region almost from the same area. The aim was to investigate the narrowest area which includes all the interfacial zones together (for a better comparison). The OM image was captured after exposure to corrosive HCl media for 30 seconds whilst the surface was previously an un-etched mirror-like polished surface with no distinguishable evidence of corrosion attack (see

also Fig. 7d, the AFM topography image with less than 0.5 µm height difference). The OM image is indicating the corrosion initiation (attack) sites around the eutectic phase. On the other side, OM and SEM images clearly show the distribution of unaffected Cu particles in the Al matrix. AFM and SKPFM could also reveal these particles marked by dashed circles. A similar phenomenon is previously observed by Galvão et al. [10] on friction stir welded Al/Cu butt joints. This is why it is believed that the temperature gradient is lower in this region in comparison with that of the S1. In addition, some diffusion bands penetrated into the Cu matrix are also observed at the vicinity of the Al/Cu interface (with the same composition of the transition zone). According to the line-profile potential measurement in the SKPFM image (Fig. 7e), the lowest real measured Volta potential value is related to Cu particles while the highest is related to its surrounding Al-rich phase. At least four potential levels could be distinguished in the SKPFM image analyzed by line-profile. Again, the highest galvanic driving force of more than 700 mV can be attributed to the Cu-rich particles embedded in the Al matrix; this is close to what Senöz et al. [49] have found previously. By a careful look at the OM image in Fig. 7b, it is obvious that the corrosion attack sites (small pits or trenches) are distributed mainly around the Cu particles and the eutectic IMCs. The last image (Fig. 7f), which reveals the histogram plot of Volta potentials, resolves a quadrumodal distribution. This is again in quite agreement with the SKPFM image in Fig. 7c and the corresponding line-profile in Fig. 7e.

Fig. 8 demonstrates the SEM images of the interfacial regions (S1 and P1) after exposure to 1 M HCl solution for 30 seconds. The typically observed flower-like primary α-Al dendrites in S1 are close to the copper lamellae beneath the shoulder (Fig. 8c and 8d). The existence of these dendrites confirms the occurrence of a local melting

and solidification process along the interface, probably due to a high difference between the melting points of Al and Cu and the relatively great amount of the heat generated in this area by the tool shoulder movement. It is believed that the Al element in contact with semi-solid Cu element can be melted locally [30-32]. Therefore, these dendrites can nucleate independently and grow directly from the nucleation sites of IMCs in the liquid phase at the edge of the deformed copper lamellae. This can be obviously observed by comparing the S1 and P1 interfacial regions. Also, it can be seen that only the primary arms of dendrites are fully developed. A similar observation which was previously reported by Ouyang et al. [6] declares that the stirring action results in the development of a low melting point hypoeutectic/eutectic Cu-Al alloy at the aluminum side and a hypereutectic alloy at the weld nugget. However, the insignificant formation of eutectic compounds in P1 might be attributed to the dominant impact of the shoulder (as a greater source of heat-input) compared to that of the pin. This may be because of the broader superficial contact (more induced friction) that is provided by the tool shoulder.

In summary, it was observed that the crumbled structure of the eutectic phase in P1 (in contrast with the S1 dendritic structure) could be directly related to the pin rotation and traverse effects. Moreover, considering the results from Fig. 8, it is obvious that the number of the preferentially attacked sites (corrosion pits) is higher in P1 (in comparison with S1) and mainly located around the dispersed Cu particles. Although, some pits are also detectable inside the Al-rich phase (adjacent to the IMCs) in both S1 and P1 regions. Finally, considering the work done by Prasad Rao *et al.* [14], due to the presence of Al and Zn elements (formation of passive products) in the transition zone, this region can be protected at initial immersion times.

4. Conclusions

Interfacial regions of a friction stir welded dissimilar lap joint of Al/Cu was characterized by a combination of diverse techniques including OM, SEM-EDS, AFM, SKPFM and Vickers micro hardness. The main conclusions can be summarized as follows:

1. Microstructure around the interface normally consisted of $CuAl_2$ IMC, α-Al phase and a transition zone that is believed to be a Cu-Al-Zn solid solution.
2. The surface constituents follow various diffusion patterns in different areas along the interface due to the various impacts of the tool pin and shoulder in dispersing the heat along the interface.
3. A local melting/solidification process also occurred at the interface because of a relatively high heat-input caused by the tool movement and a considerable difference between the Al and Cu melting points (c.a. 400°C).
4. Due to the higher impact of the shoulder and the consequential more severe plastic deformation, hardness values in the S1 region were notably higher than those of the region around the pin.
5. Concerning the Volta potential distribution by SKPFM, a multimodal Gaussian distribution was also employed to characterize the surface potential patterns and correlate the results to the microstructural identifications provided by SEM-EDS technique.
6. Surface topography was performed by utilizing AFM to confirm the observations by other characterization methods.

7. Finally, it was observed that the localized corrosion initiated from those regions with relatively the highest difference in real measured Volta potential values (i.e. the interface of Al-rich phases and dispersed Cu particles in the P1 region).

Acknowledgements

The authors would like to acknowledge the Ferdowsi University of Mashhad and Hakim Sabzevari University for financial support and providing experimental facilities. In addition, Mrs. M. Sadeghian's technical assistance regarding the Scanning Electron Microscopy is appreciated.

References

[1] M. Peel, A. Steuwer, M. Preuss, P.J. Withers, Microstructure, mechanical properties and residual stresses as a function of welding speed in aluminium AA5083 friction stir welds, Acta Mater. 51 (2003) 4791-4801.

[2] P. Xue, B.L. Xiao, Z.Y. Ma, Enhanced strength and ductility of friction stir processed Cu–Al alloys with abundant twin boundaries, Scr. Mater. 68 (2013) 751-754.

[3] R.S. Mishra, Z.Y. Ma, Friction stir welding and processing, Mater. Sci. Eng., R 50 (2005) 1-78.

[4] L.E. Murr, R.D. Flores, O.V. Flores, J.C. McClure, G. Liu, D. Brown, Friction-stir welding: microstructural characterization, Mater. Res. Innovations 1 (1998) 211-223.

[5] L.E. Murr, Y. Li, R.D. Flores, E.A. Trillo, J.C. McClure, Intercalation vortices and related microstructural features in the friction-stir welding of dissimilar metals, Mater. Res. Innovations 2 (1998) 150-163.

[6] J. Ouyang, E. Yarrapareddy, R. Kovacevic, Microstructural evolution in the friction stir welded 6061 aluminum alloy (T6-temper condition) to copper, J. Mater. Process. Technol. 172 (2006) 110-122.

[7] T. Khaled, An outsider looks at friction stir welding, Federal Aviation Administration Report: ANM-112N-05-06, (2005).

[8] T. Saeid, A. Abdollah-zadeh, B. Sazgari, Weldability and mechanical properties of dissimilar aluminum–copper lap joints made by friction stir welding, J. Alloys Compd. 490 (2010) 652-655.

[9] P. Xue, B.L. Xiao, D.R. Ni, Z.Y. Ma, Enhanced mechanical properties of friction stir welded dissimilar Al–Cu joint by intermetallic compounds, Mater. Sci. Eng., A 527 (2010) 5723-5727.

[10] I. Galvão, J.C. Oliveira, A. Loureiro, D.M. Rodrigues, Formation and distribution of brittle structures in friction stir welding of aluminium and copper: Influence of shoulder geometry, Intermetallics 22 (2012) 122-128.

[11] A. Abdollah-Zadeh, T. Saeid, B. Sazgari, Microstructural and mechanical properties of friction stir welded aluminum/copper lap joints, J. Alloys Compd. 460 (2008) 535-538.

[12] A. Elrefaey, M. Takahashi, K. Ikeuchi, Preliminary Investigation of Friction Stir Welding Aluminium/Copper Lap Joints, Weld. World 49 (2013) 93-101.

[13] C.Y. Chen, H.L. Chen, W.S. Hwang, Influence of interfacial structure development on the fracture mechanism and bond strength of aluminum/copper bimetal plate, Mater. Trans. 47 (2006) 1232-1239.

[14] K. Prasad Rao, G.D. Janaki Ram, B.E. Stucker, Effect of friction stir processing on corrosion resistance of aluminum–copper alloy gas tungsten arc welds, Mater. Des. 31 (2010) 1576-1580.

[15] K.S. Rao, K.P. Rao, Microstructure and pitting corrosion of partially melted zones of Al alloy GTA welds, Mater. Sci. Technol. 21 (2005) 1199-1208.

[16] X. Feng, H. Liu, S. Suresh Babu, Effect of grain size refinement and precipitation reactions on strengthening in friction stir processed Al–Cu alloys, Scr. Mater. 65 (2011) 1057-1060.

[17] J.H.W. de Wit, Local potential measurements with the SKPFM on aluminium alloys, Electrochim. Acta 49 (2004) 2841-2850.

[18] L.Q. Guo, X.M. Zhao, Y. Bai, L.J. Qiao, Water adsorption behavior on metal surfaces and its influence on surface potential studied by in situ SPM, Appl. Surf. Sci. 258 (2012) 9087-9091.

[19] M. Li, L.Q. Guo, L.J. Qiao, Y. Bai, The mechanism of hydrogen-induced pitting corrosion in duplex stainless steel studied by SKPFM, Corros. Sci. 60 (2012) 76-81.

[20] B. Maachi, C. Pirri, A. Mehdaoui, N.E. Hakiki, J.L. Bubendorff, Atomic Force Microscopy, Scanning Kelvin Probe Force Microscopy and magnetic measurements on thermally oxidized AISI 304 and AISI 316 stainless steels, Corros. Sci. 53 (2011) 984-991.

[21] N. Sathirachinda, R. Pettersson, J. Pan, Depletion effects at phase boundaries in 2205 duplex stainless steel characterized with SKPFM and TEM/EDS, Corros. Sci. 51 (2009) 1850-1860.

[22] N. Sathirachinda, R. Pettersson, S. Wessman, J. Pan, Study of nobility of chromium nitrides in isothermally aged duplex stainless steels by using SKPFM and SEM/EDS, Corros. Sci. 52 (2010) 179-186.

[23] B.S. Tanem, G. Svenningsen, J. Mårdalen, Relations between sample preparation and SKPFM Volta potential maps on an EN AW-6005 aluminium alloy, Corros. Sci. 47 (2005) 1506-1519.

[24] H.K. Wickramasinghe, Progress in scanning probe microscopy, Acta Mater. 48 (2000) 347-358.

[25] T. Li, K. Zeng, Piezoelectric properties and surface potential of green abalone shell studied by scanning probe microscopy techniques, Acta Mater. 59 (2011) 3667-3679.

[26] L.Q. Guo, X.M. Zhao, B.C. Wang, Y. Bai, B.Z. Xu, L.J. Qiao, The initial stage of atmospheric corrosion on interstitial free steel investigated by in situ SPM, Corros. Sci. 70 (2013) 188-193.

[27] A. Steuwer, M. Dumont, J. Altenkirch, S. Birosca, A. Deschamps, P.B. Prangnell, P.J. Withers, A combined approach to microstructure mapping of an Al–Li AA2199 friction stir weld, Acta Mater. 59 (2011) 3002-3011.

[28] A.B. Cook, Z. Barrett, S.B. Lyon, H.N. McMurray, J. Walton, G. Williams, Calibration of the scanning Kelvin probe force microscope under controlled environmental conditions, Electrochim. Acta 66 (2012) 100-105.

[29] Y.S. Sato, M. Urata, H. Kokawa, K. Ikeda, Hall–Petch relationship in friction stir welds of equal channel angular-pressed aluminium alloys, Mater. Sci. Eng., A 354 (2003) 298-305.

[30] I. Galvão, R.M. Leal, D.M. Rodrigues, A. Loureiro, Influence of tool shoulder geometry on properties of friction stir welds in thin copper sheets, J. Mater. Process. Technol. 213 (2013) 129-135.

[31] H. Schmidt, J. Hattel, J. Wert, An analytical model for the heat generation in friction stir welding, Modelling and Simulation in Mater. Sci. Eng. 12 (2004) 143-157.

[32] R. Nandan, T. Debroy, H. Bhadeshia, Recent advances in friction-stir welding – Process, weldment structure and properties, Prog. Mater. Sci. 53 (2008) 980-1023.

[33] R. Beygi, M. Kazeminezhad, A.H. Kokabi, Butt joining of Al–Cu bilayer sheet through friction stir welding, Transactions of Nonferrous Metals Society of China, 22 (2012) 2925-2929.

[34] A. Esmaeili, M.K.B. Givi, H.R.Z. Rajani, A metallurgical and mechanical study on dissimilar Friction Stir welding of aluminum 1050 to brass (CuZn30), Mater. Sci. Eng., A 528 (2011) 7093-7102.

[35] M.S. Moghaddam, R. Parvizi, M. Haddad-Sabzevar, A. Davoodi, Microstructural and mechanical properties of friction stir welded Cu–30Zn brass alloy at various feed speeds: Influence of stir bands, Mater. Des. 32 (2011) 2749-2755.

[36] X.-w. Li, D.-t. Zhang, C. Qiu, W. Zhang, Microstructure and mechanical properties of dissimilar pure copper/1350 aluminum alloy butt joints by friction stir welding, Transactions of Nonferrous Metals Society of China, 22 (2012) 1298-1306.

[37] G. Pouget, A.P. Reynolds, Residual stress and microstructure effects on fatigue crack growth in AA2050 friction stir welds, Int. J. Fatigue 30 (2008) 463-472.

[38] D. Hull, D.J. Bacon, Introduction to Dislocations, Elsevier Science, 2001.

[39] G.E. Dieter, Mechanical metallurgy, McGraw-Hill, 1976.

[40] A. Kelly, G.W. Groves, P. Kidd, Crystallography and Crystal Defects, Wiley, 2000.

[41] V. Raghavan, Phase diagram evaluations: Section 2, J. Phase Equilib. Diffus. 12 (1991) 550-550.

[42] Smithells Metals Reference Book Seventh ed., Butterworth-Heinemann, 2003.

[43] W.F. Xu, J.H. Liu, D.L. Chen, Material flow and core/multi-shell structures in a friction stir welded aluminum alloy with embedded copper markers, J. Alloys Compd. 509 (2011) 8449-8454.

[44] P. Fellner, M. Chrenkova-Paucirova, Kinetics of formation of diffusion layer at the electrolytic deposition of aluminium on copper base from molten electrolyte, Chem. Pap. - Chem. Zvesti 36 (1982) 321-325.

[45] A. Davoodi, J. Pan, C. Leygraf, R. Parvizi, S. Norgren, An insight into the influence of morphological and compositional heterogeneity of an individual intermetallic particle on aluminium alloy corrosion initiation, Mater. Corros. 64 (2013) 195-198.

[46] S. Varadarajan, R.A. Fournelle, Low temperature volume diffusion of zinc in aluminium, Acta Metall. Mater. 40 (1992) 1847-1854.

[47] S. Guerdoux, L. Fourment, A 3D numerical simulation of different phases of friction stir welding, Modelling and Simulation in Mater. Sci. Eng. 17 (2009) 075001.

[48] M. Sababi, S. Ejnermark, J. Andersson, P.M. Claesson, J. Pan, Microstructure influence on corrosion behavior of a Fe–Cr–V–N tool alloy studied by SEM/EDS, scanning Kelvin force microscopy and electrochemical measurement, Corros. Sci. 66 (2013) 153-159.

[49] C. Senöz, S. Borodin, M. Stratmann, M. Rohwerder, In situ detection of differences in the electrochemical activity of Al_2Cu IMPs and investigation of their effect on FFC by scanning Kelvin probe force microscopy, Corros. Sci. 58 (2012) 307-314.

[50] S.C. Nagpure, S.S. Babu, B. Bhushan, A. Kumar, R. Mishra, W. Windl, L. Kovarik, M. Mills, Local electronic structure of $LiFePO_4$ nanoparticles in aged Li-ion batteries, Acta Mater. 59 (2011) 6917-6926.

[51] A. Davoodi, J. Pan, C. Leygraf, S. Norgren, Integrated AFM and SECM for in situ studies of localized corrosion of Al alloys, Electrochim. Acta 52 (2007) 7697-7705.

[52] S. Zheng, C. Li, Y. Qi, L. Chen, C. Chen, Mechanism of (Mg,Al,Ca)-oxide inclusion-induced pitting corrosion in 316L stainless steel exposed to sulphur environments containing chloride ion, Corros. Sci. 67 (2013) 20-31.

Figure captions:

Figure 1 (a) Schematic illustration of the FSW process. The right part shows an inserted cross-section image of the welded sample, (b) SEM-BSE image of the interface studied in this survey. The P1 and P2 regions point to the interface around the pin and the S1 region refers to the interface beneath the shoulder.

Figure 2 Hardness profile along with straight lines in the P1 and S1 regions, introduced in Fig. 1, demonstrating the studied regions around the pin and beneath the shoulder, respectively.

Figure 3 SEM-EDS (BSE) line-scan around the interfacial region illustrating Al, Cu, and Zn elements (in at%) scattered along a line across the interfaces. The red, green and blue colors indicate Cu, Al and the Zn elements, respectively. (a) Element distribution in the P1 region, (b) greater magnification of Fig. 3a and (c) distribution of the elements in the S1 region.

Figure 4 (a) SEM-EDS analysis of the Al/Cu interface in the P2 region, (a) measured spectrum points, (b) bar-chart comparing the chemical composition (in at%) variations of spectrum 1 to 9.

Figure 5 (a-g) Seven sequential SKPFM images of the Al/Cu interface in the P1 region, (h) AFM camera view of the boundary in P1 region, (i) Histogram plots of all seven SKPFM images, (j) an example of a simulated multinomial (quinquemodal) Gaussian distribution of the histogram plot corresponding to the zone (f).

Figure 6 (a-f) Six sequential SKPFM images of the Al/Cu interface in the S1 region, (g) corresponding histogram plots of all six SKPFM images, and (h) an example of the

simulated multinomial (quadrumodal) Gaussian distribution of the histogram plot corresponding to the zone (c).

Figure 7 (a-d) SEM, OM, SKPFM and AFM images of the Al/Cu interface in the P2 region, (e) Volta potential line-profile record on Fig. 7c and (f) the histogram plot and the simulated multinomial (quadrumodal) Gaussian distribution corresponding to Fig. 7.c.

Figure 8 SEM images of the Al/Cu interfaces after exposure to 1 M HCl solution for 30 seconds, (a, b) the P1 region, around the pin, and (c, d) the S1 region, beneath the shoulder.

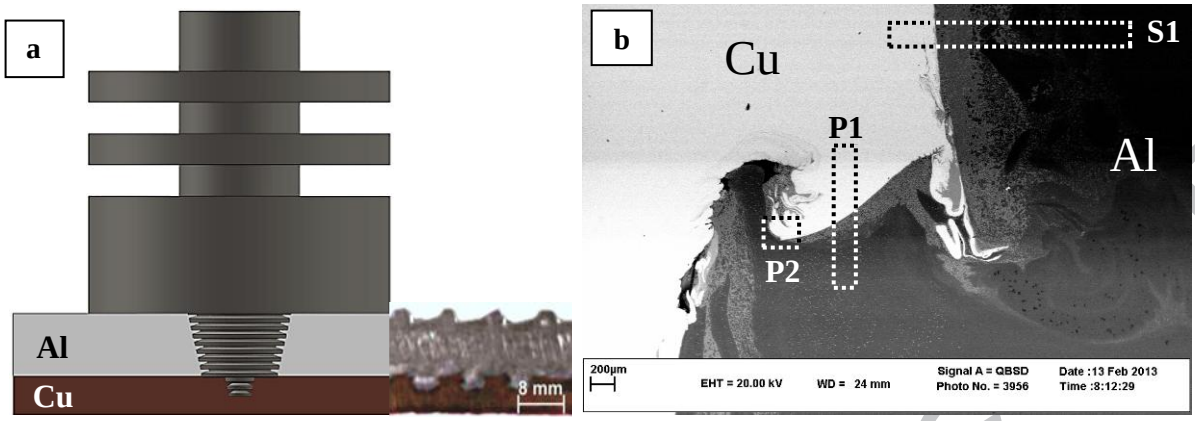

Figure 1

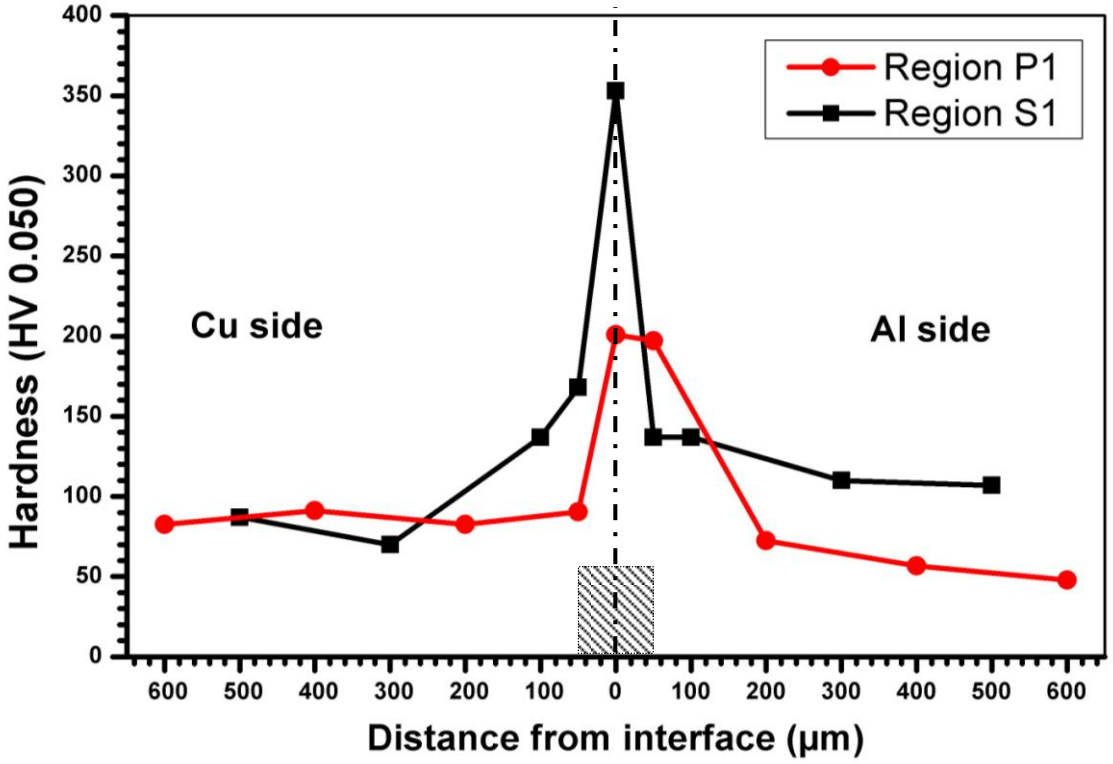

Figure 2

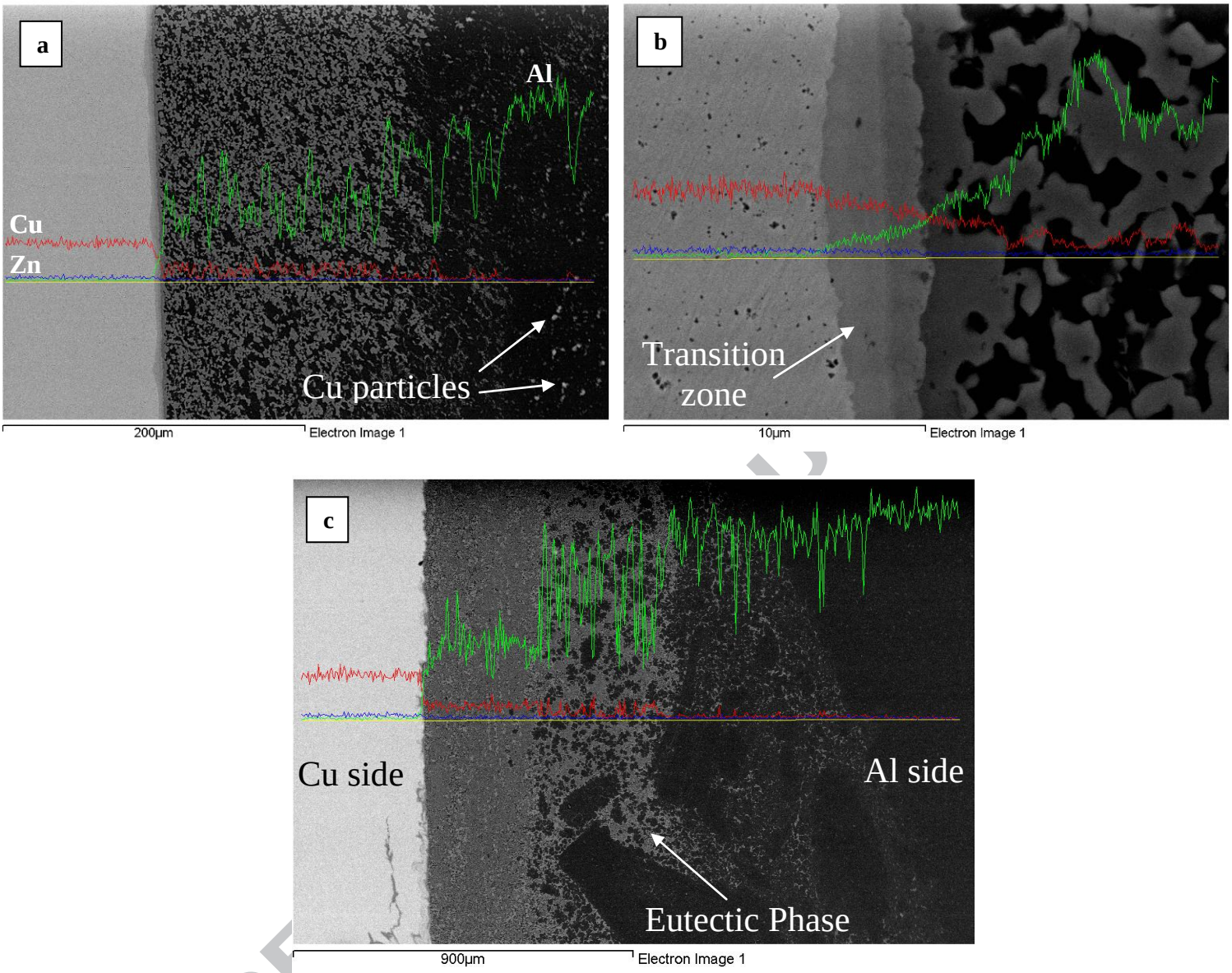

Figure 3

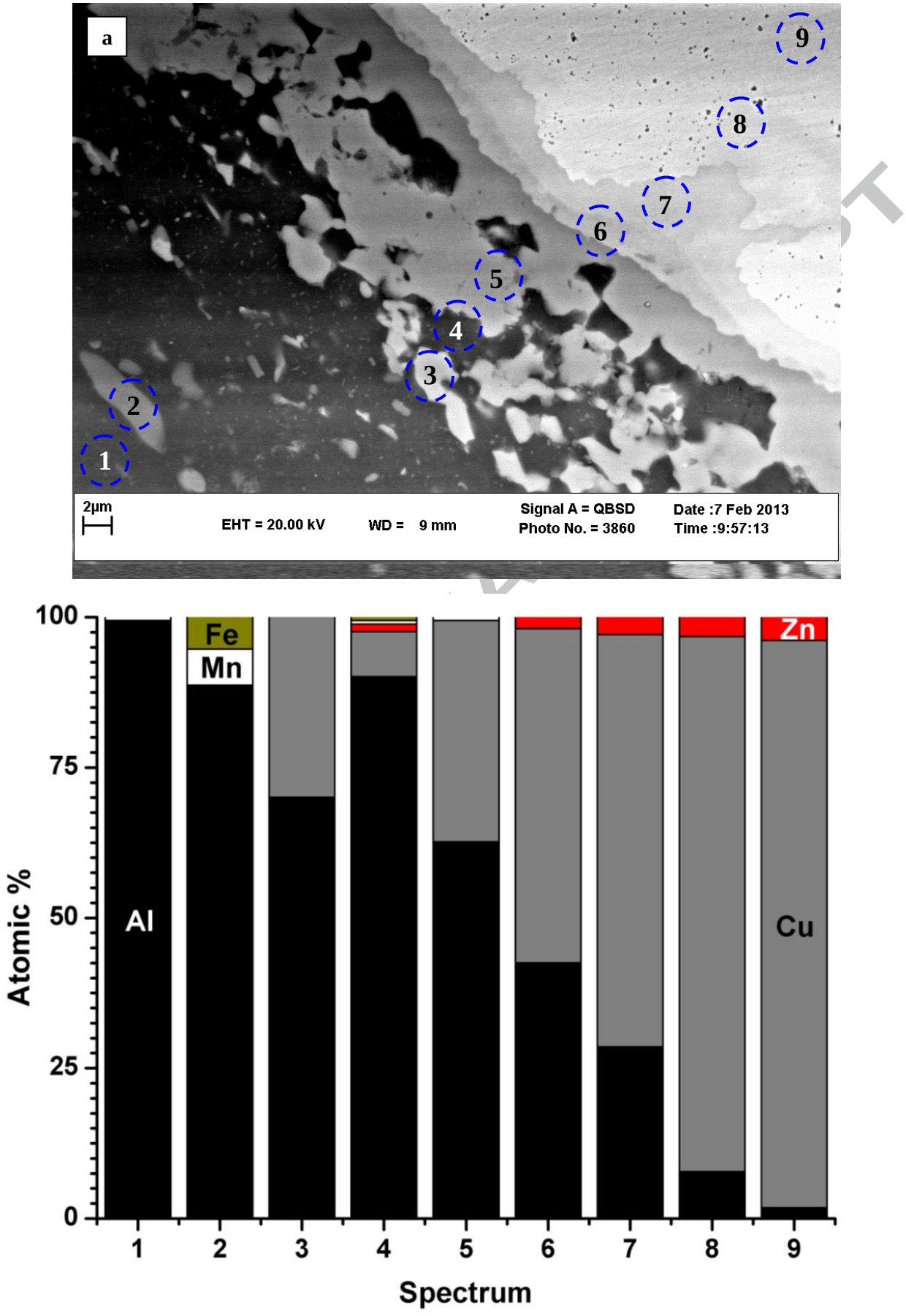

Figure 4

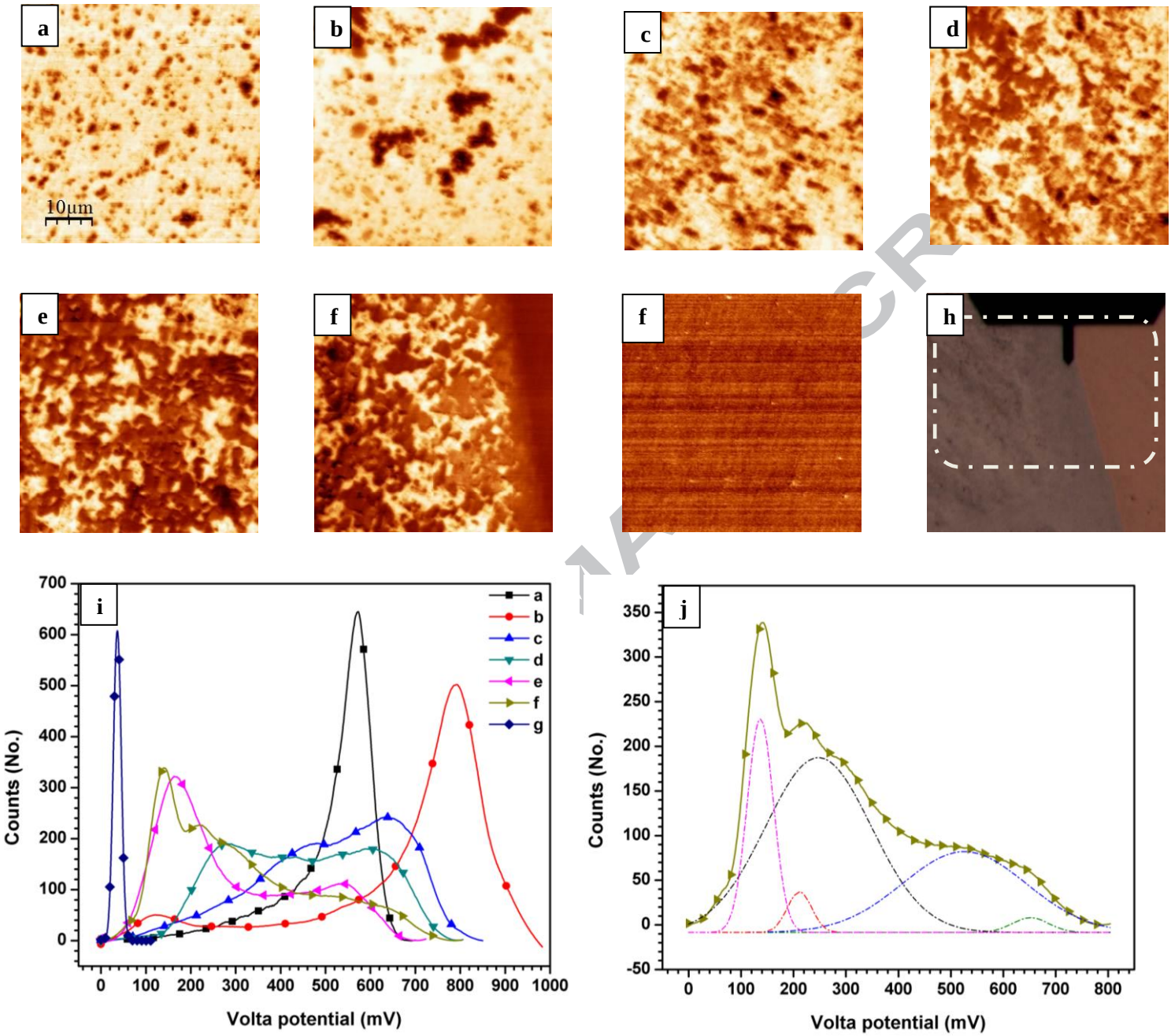

Figure 5

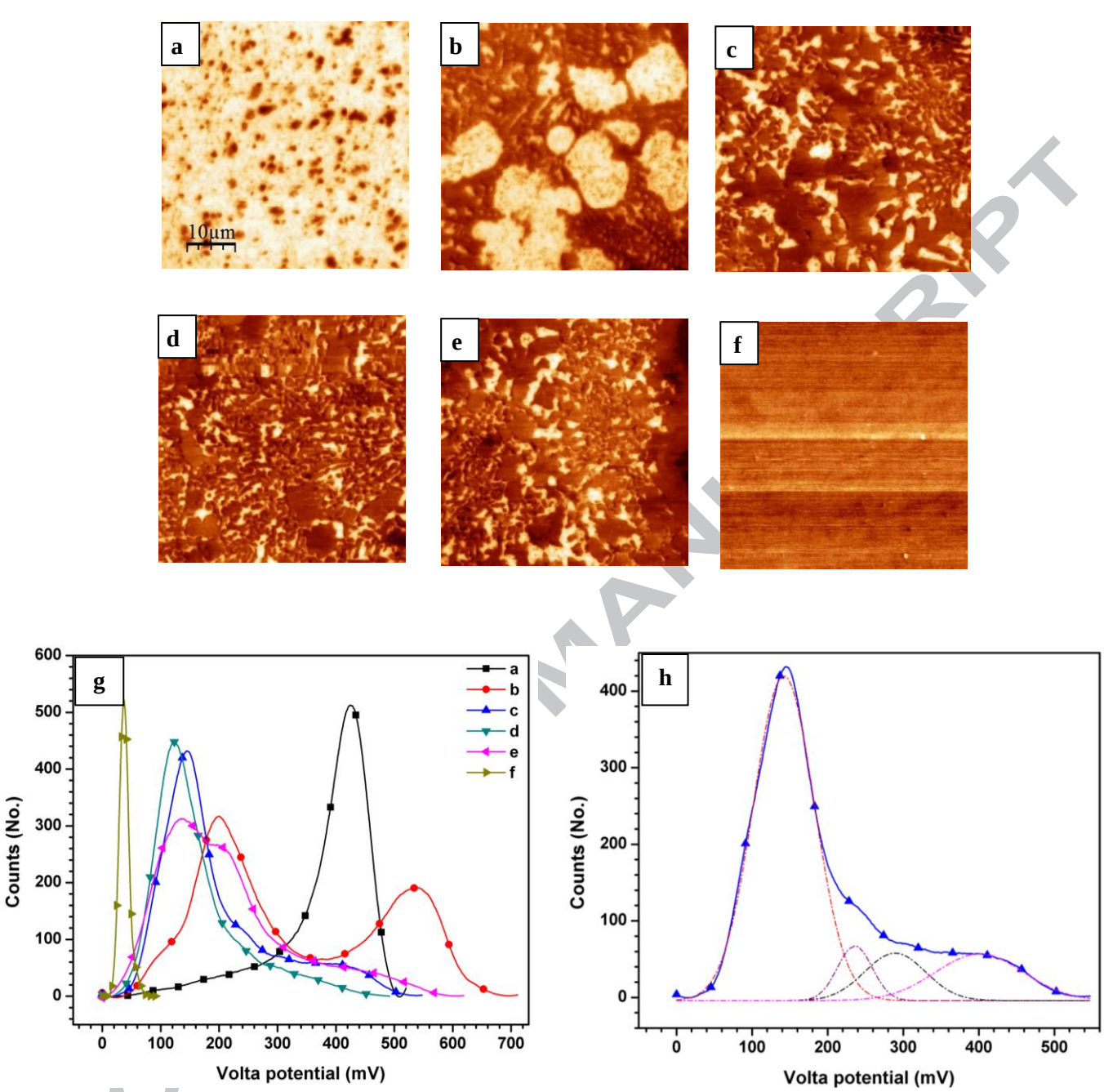

Figure 6

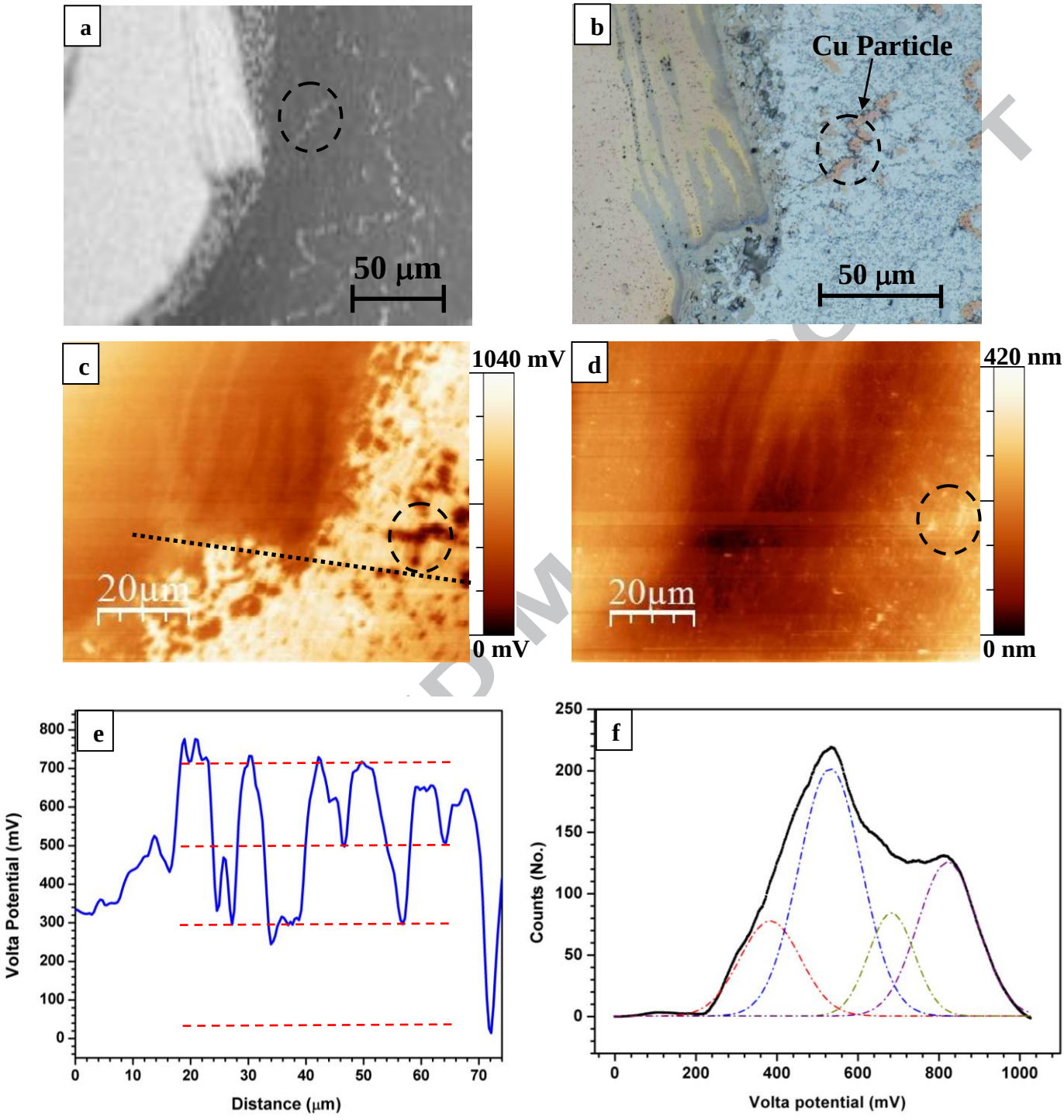

Figure 7

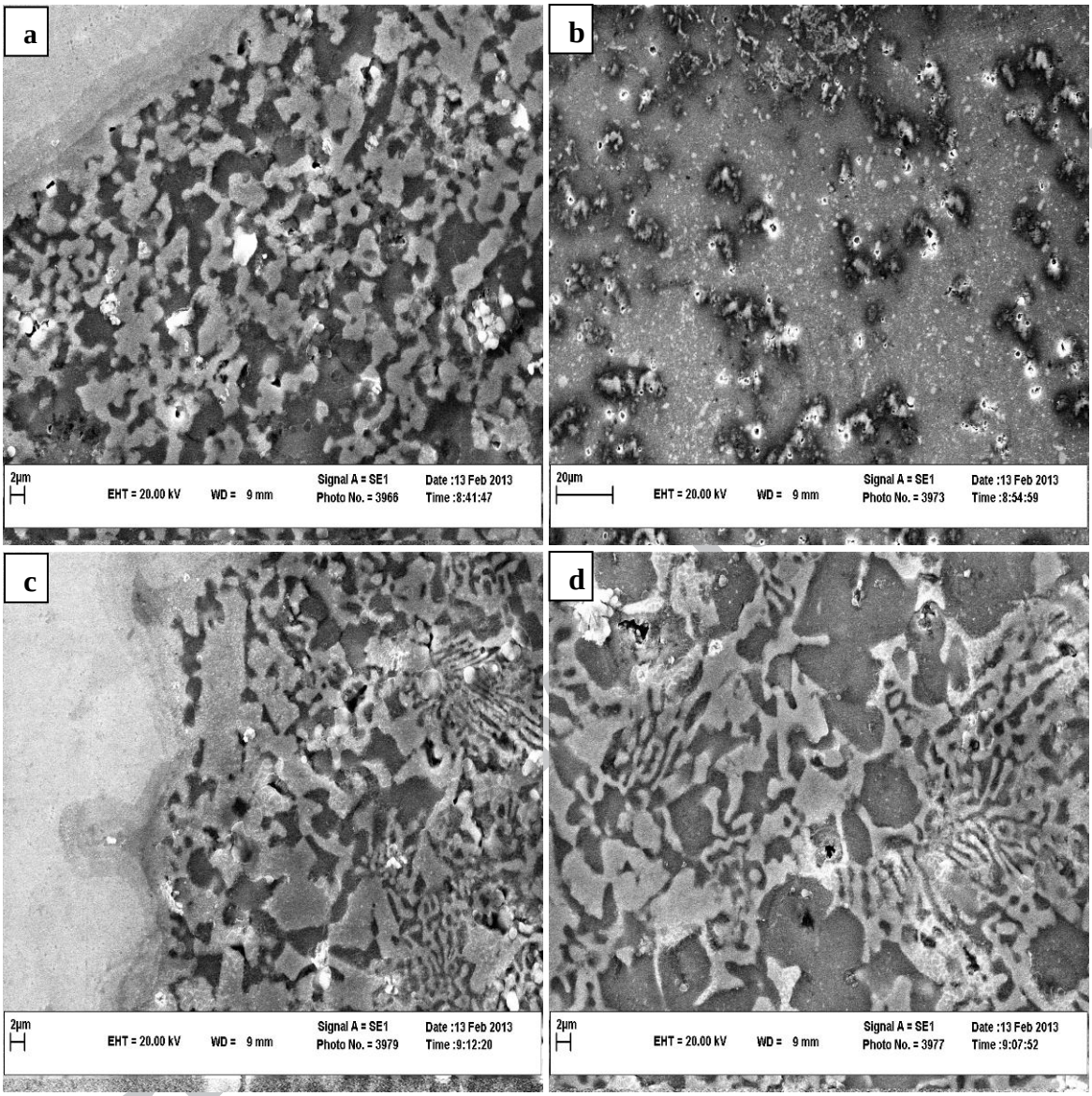

Figure 8

Spectrum No.	Chemical composition (at%)
1	99.48% **Al** + 0.52% **Mn**
2	88.69% **Al** + 6% **Mn** + 5.31% **Fe**
3	70.05% **Al** + 29.95% **Cu**
4	90.11% **Al** + 0.61% **Mn** + 0.53% **Fe** + 7.51% **Cu** + 1.24% **Zn**
5	62.63% **Al** + 0.54% **Mn** + 36.83% **Cu**
6	42.52% **Al** + 55.57% **Cu** + 1.91% **Zn**
7	28.54% **Al** + 68.54% **Cu** + 2.92% **Zn**
8	7.81% **Al** + 88.95% **Cu** + 3.24% **Zn**
9	1.80% **Al** + 94.31% **Cu** + 3.89% **Zn**

Table 1 chemical composition of each spectrum (in at%) defining elemental composition by moving from Al to the Cu matrix.

Region label	Histogram label	Minimum number of modals	Mean value (μ, mV)	Standard deviation (σ, mV)	Max. driving force ($\Delta\mu = \mu_{max} - \mu_{min}$)
P1 (Fig. 5i)	a	3	μ_1= 575	σ_1= 55	575 – 423 = 152
			μ_2= 529	σ_2= 95	
			μ_3= 423	σ_3= 219	
	b	3	μ_1= 792	σ_1= 105	792 – 136 = 656
			μ_2= 699	σ_2= 233	
			μ_3= 136	σ_3= 76	
	c	4	μ_1= 708	σ_1= 57	708 – 222 = 486
			μ_2= 651	σ_2= 135	
			μ_3= 470	σ_3= 227	
			μ_4= 222	σ_4= 187	
	d	4	μ_1= 660	σ_1= 93	660 – 256 = 404
			μ_2= 578	σ_2= 130	
			μ_3=397	σ_3= 221	
			μ_4= 256	σ_4= 105	
	e	3	μ_1= 538	σ_1= 148	538 – 164 = 374
			μ_2= 309	σ_2= 232	
			μ_3= 164	σ_3= 105	
	f	5	μ_1= 651	σ_1= 69	651 – 136 = 515
			μ_2= 525	σ_2= 235	
			μ_3=247	σ_3= 201	
			μ_4= 211	σ_4= 46	
			μ_5= 136	σ_5= 50	
	g	1	μ_1= 36	σ_1= 17	
S1 (Fig. 6g)	a	3	μ_1= 429	σ_1= 56	429 – 264 = 165
			μ_2= 381	σ_2= 86	
			μ_3= 264	σ_3= 204	
	b	3	μ_1= 535	σ_1= 96	535 – 202 = 333
			μ_2= 397	σ_2= 188	
			μ_3= 202	σ_3= 109	
	c	3	μ_1= 411	σ_1= 114	411 – 137 = 274
			μ_2= 219	σ_2= 170	
			μ_3= 137	σ_3= 72	
	d	3	μ_1= 256	σ_1= 208	256 – 118 = 138
			μ_2= 156	σ_2= 94	
			μ_3= 118	σ_3= 61	
	e	4	μ_1= 413	σ_1= 210	413 – 125 = 288
			μ_2= 222	σ_2= 147	
			μ_3= 216	σ_3= 57	
			μ_4= 125	σ_4 = 92	
	f	1	μ_1= 36	σ_1= 15	
P2 (Fig. 7f)		4	μ_1= 821	σ_1= 147	821 – 383 = 438
			μ_2= 682	σ_2= 113	
			μ_3= 531	σ_3= 154	
			μ_4= 383	σ_4= 149	

Table 2 extracted multimodal Gaussian distribution parameters from the Volta potential histograms.

Research highlights

- Interfaces of FS welded Al/Cu joint was characterized by OM, SEM, AFM and SKPFM.
- A eutectic phase mainly consisting of $CuAl_2$ IMC and an Al-rich phase was detected.
- Severe mechanical deformation caused a concurrent depletion/enrichment mechanism.
- A correlation between phases and their Volta potential distribution is found.
- Corrosion initiated from sites with relatively higher absolute Volta potentials.

Graphical abstract

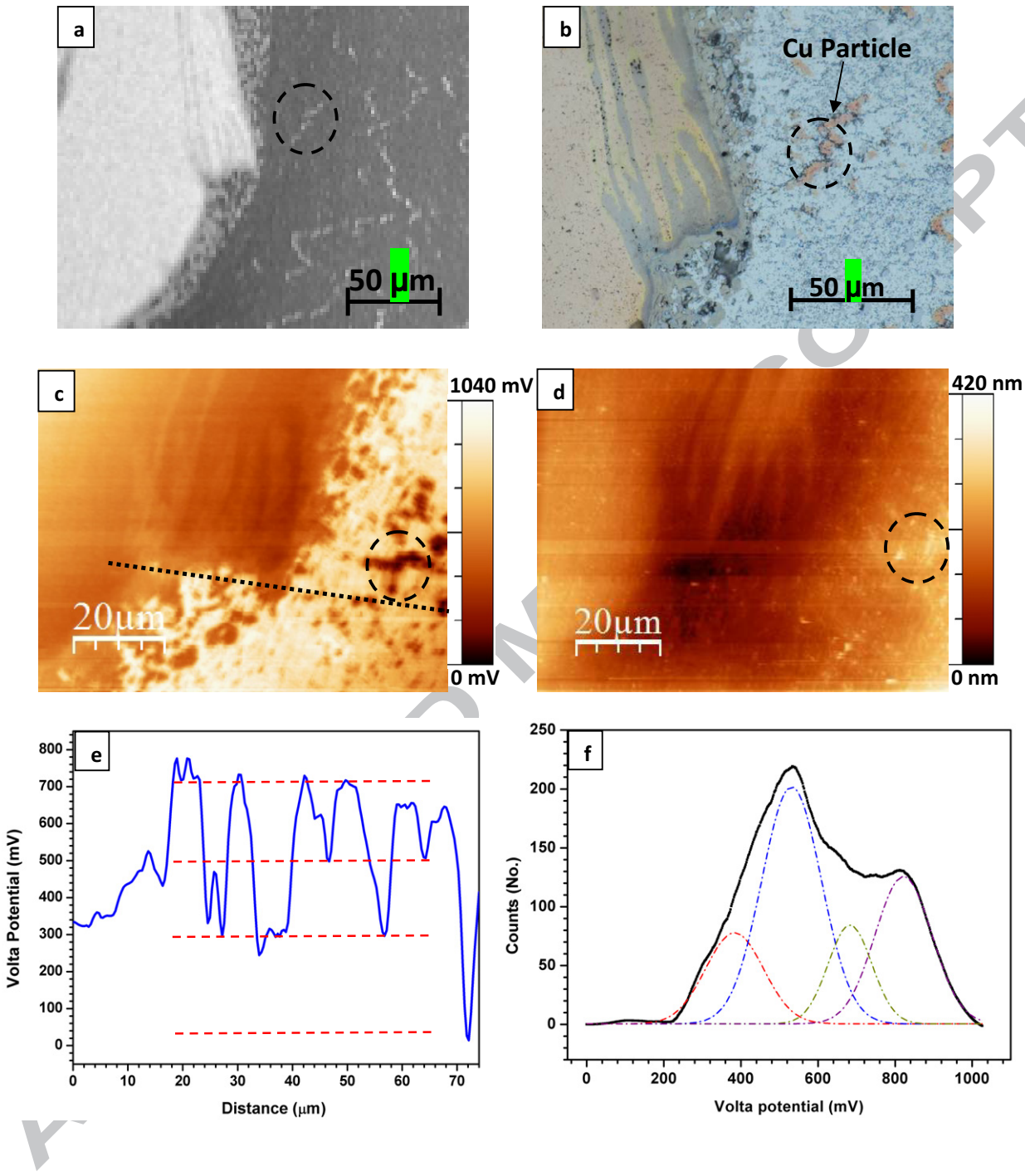

Interfacial microstructure characterization of an aluminum/copper friction stir weld:

(a-d) SEM, OM, SKPFM and AFM images of Al/Cu interface around the tool pin, (e) Volta potential line-profile record on the SKPFM result, and (f) histogram plot and simulated

multinomial Gaussian distribution corresponding to image (e). It is notable that all images demonstrate the same area from different points of view.